Osteogenic lithium-doped brushite cements for bone regeneration

K. Hurle [a,*], F.R. Maia [b,c], V.P. Ribeiro [b,c], S. Pina [b,c], J.M. Oliveira [b,c], F. Goetz-Neunhoeffer [a], R. L. Reis [b,c,**]

[a] *GeoZentrum Nordbayern, Mineralogy, Friedrich-Alexander University Erlangen-Nürnberg (FAU), 91054, Erlangen, Germany*
[b] *3B's Research Group, I3Bs – Research Institute on Biomaterials, Biodegradables and Biomimetics, University of Minho, Headquarters of the European Institute of Excellence on Tissue Engineering and Regenerative Medicine, AvePark, Parque de Ciência e Tecnologia, Zona Industrial da Gandra, 4805-017, Barco, Guimarães, Portugal*
[c] *ICVS/3B's–PT Government Associate Laboratory, Braga, Guimarães, Portugal*

ARTICLE INFO

ABSTRACT

This study investigated the osteogenic performance of new brushite cements obtained from Li$^+$-doped β-tricalcium phosphate as a promising strategy for bone regeneration. Lithium (Li$^+$) is a promising trace element to encourage the migration and proliferation of adipose-derived stem cells (hASCs) and the osteogenic differentiation-related gene expression, essential for osteogenesis. *In-situ* X-ray diffraction (XRD) and *in-situ* ^{1}H nuclear magnetic resonance (^{1}H NMR) measurements proved the precipitation of brushite, as main phase, and monetite, indicating that Li$^+$ favored the formation of monetite under certain conditions. Li$^+$ was detected in the remaining pore solution in significant amounts after the completion of hydration. Isothermal calorimetry results showed an accelerating effect of Li$^+$, especially for low concentration of the setting retarder (phytic acid). A decrease of initial and final setting times with increasing amount of Li$^+$ was detected and setting times could be well adjusted by varying the setting retarder concentration. The cements presented compressive mechanical strength within the ranges reported for cancellous bone. *In vitro* assays using hASCs showed normal metabolic and proliferative levels. The immunodetection and gene expression profile of osteogenic-related markers highlight the incorporation of Li$^+$ for increasing the *in vivo* bone density. The osteogenic potential of Li-doped brushite cements may be recommended for further research on bone defect repair strategies.

1. Introduction

Bone defects induced by fractures, infection, or diseases are still challenging to the current gold standard treatment of bone repair [1]. Internal fixation, autografts and allografts are the main treatments used for the repair and regeneration of bone disorders [2]. Several shortcomings of these approaches are related to infection, risk of disease transfer, chronic donor site pain, potential immunogenicity, and insufficient donor tissue supply, therefore justifying the continuous research effort in the development of biomimetic materials [3,4].

Calcium phosphate cements (CPCs) have been widely used as bone graft substitutes and as drug delivery systems [5,6]. These materials possess high biocompatibility, resorbability, and osteoconductivity and are particularly suited for minimally invasive surgical techniques, hardening in situ and providing stability for any defect geometry. Depending on their final hydration product at 37 °C, CPCs can be designated as apatite or brushite (CaHPO$_4$·2H$_2$O) cements [7,8]. Apatite is formed when the pH value of the cement paste is above 4.2, while brushite is preferentially formed for pH < 4.2. Compared to apatite, brushite cements have higher resorbability under physiological conditions, thus allowing a faster replacement by newly formed bone [9].

Brushite cements can be obtained by mixing β-tricalcium phosphate (β-Ca$_3$(PO$_4$)$_2$, β-TCP) with monocalcium phosphate monohydrate (Ca (H$_2$PO$_4$)$_2$·H$_2$O, MCPM) and H$_2$O, resulting in the reaction according to Eq. (1) [10].

$$\beta-Ca_3(PO_4)_2 \ + \ Ca(H_2PO_4)_2 \cdot H_2O \ + \ 7 \ H_2O \xrightarrow{\ H_2O\ } 4 \ CaHPO_4 \cdot 2H_2O \tag{1}$$

The formation of monetite ($CaHPO_4$) is also possible under certain conditions, as shown in Eq. (2) [11].

$$\beta-Ca_3(PO_4)_2 \ + \ Ca(H_2PO_4)_2 \cdot H_2O \xrightarrow{\ H_2O\ } 4 \ CaHPO_4 \ + \ H_2O \tag{2}$$
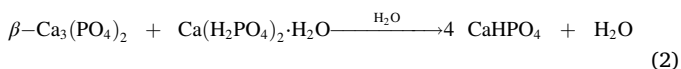
Different retarders have been used to adjust the setting time of brushite cements to clinical needs, such as citric acid [12] or phytic acid (inositol hexaphosphate, $C_6H_{18}O_{24}P_6$, IP6) [13]. IP6 has the benefit to remarkably improve the cement paste injectability and adjust the reaction times for favorable setting and rheology performances. This is highly relevant with respect to minimally invasive applications, where the cement is inserted into the defect site by a syringe with a narrow cannula [13].

The presence of ionic dopants in bioceramics and cements has gained relevance in enhancing their mechanical properties and accelerating bone turnover, particularly bone resorption resulting from the induced calcium deficiency [12,14–18]. β-TCP can incorporate a number of divalent ions, like Mg^{2+} [19], Sr^{2+} [20], Zn^{2+} [21] or Cu^{2+} [22], by simply replacing one Ca^{2+} ion. These ions are released during the dissolution of β-TCP in the liquid phase. However, the substitution is also possible for monovalent ions if charge compensation is ensured. The rhombohedral β-TCP structure contains five different Ca positions. The occupancy of Ca(4) is around 0.5 [23,24], while the others are fully occupied. Yoshida et al. [25] described a substitution mechanism for monovalent alkali ions (Li^+, Na^+, K^+), with one Ca(4) site and one vacancy $V_{Ca(4)}$ being replaced by two monovalent ions according to $2 \ M^+ \leftrightarrow Ca^{2+} + V_{Ca(4)}$. Assuming that all vacancies are filled, the theoretical substitution limit is 9.1 mol%, which is in accordance with their experimental results.

Li^+ incorporation has been shown to stimulate bone formation and induce proangiogenesis by eliciting the expression of exosomes [26,27]. Li^+ inhibits the negative regulator of Wnt (Wingless-related integration site denotes genes belonging to the INT1/Wingless family) signaling pathway and activates β-catenin-medicated T cell factor, increasing bone formation [28]. Chen et al. [29] reported that Li-calcium silicate bioceramics significantly promoted cartilage and subchondral bone regeneration in rabbit osteochondral defects. Similarly, Li et al. [30] showed that Li-doped CPC meaningfully improved osteoblast proliferation and differentiation.

Therefore, considering the possible positive effects of Li^+, we hypothesized that Li^+ containing brushite cements might show interesting biological properties for future applications in bone regeneration. In this study, a detailed impact of Li^+ incorporation into β-TCP on the hydration mechanism of brushite cements was investigated. The physicochemical characterization included particle size analysis of the β-TCP powders, quantitative phase analysis by (in-situ) X-ray diffraction (XRD) and Rietveld refinement, in-situ ^1H NMR measurements, isothermal calorimetry, pore water analysis, ion release, and setting times measurements. The mechanical strength of the cements was also determined. Additionally, the in vitro proliferation and differentiation responses of human adipose-derived stem cells (hASCs) cultured on the powdered cements were investigated, including metabolic activity and proliferation, alkaline phosphatase (ALP) activity, collagen expression, and quantification of mRNA levels of the osteogenic-related markers ALP, collagen Type-I (Col Iα), osteopontin (OPN), osteocalcin (OCN), Runt-related transcription factor 2 (Runx), and bone sialoprotein (BSP).

2. Materials and methods

2.1. Preparation of Li^+-doped β-TCP powders and brushite cements

The β-TCP powders were fabricated by solid-state sintering from $CaCO_3$ (Sigma Aldrich, Steinheim, Germany), $CaHPO_4$, and Li_2CO_3 (both Alfa Aesar, Heysham, Lancashire, United Kingdom). Li^+ was added in concentrations of 2.5 and 5 mol% related to the Ca^{2+} content, assuming a substitution mechanism $Ca^{2+} \leftrightarrow 2 \ Li^+$ [25]. The starting powders were homogenized in a vibratory disc mill RS1 (Retsch, Haan, Germany) with an agate grinding jar and then heat-treated in platinum crucibles at 1,000 ± 20 °C in a chamber furnace (Nabertherm 1400 GmbH, Lilienthal, Germany) for 16 h. The calcined powders were milled two times for 2 min, plus 5 min in a disc mill. They were designated as Li2.5-TCP and Li5-TCP respectively for 2.5 and 5 mol% of Li^+. Pure β-TCP (TCP) was prepared for comparison purposes.

The cements were fabricated by means of mixing TCP, Li2.5-TCP, or Li5-TCP with MCPM (Sigma Aldrich, Steinheim, Germany) in a molar ratio of 1:1, with a liquid-to-powder ratio (LPR) of 0.3 ml/g. Two different aqueous solutions of 3 wt% and 0.75 wt% IP6 (Sigma Aldrich, Steinheim, Germany), related to the powder of the mixed cement paste, were used as mixing liquid. A higher IP6 concentration was used to obtain slow reactions to enable a detailed investigation of the setting/hydration mechanism. In comparison, a lower IP6 concentration yielded cement pastes with setting performance close to the clinical standard requirements. The cement pastes were designated as Li2.5-BrC and Li5–BrC, respectively, for 2.5 and 5 mol% of Li^+ content. Pure brushite cement (BrC) was prepared for comparison purposes. If not explicitly described otherwise, all cement pastes were prepared by manual stirring with a metal spatula for 1 min.

2.2. Physicochemical characterization of the powders and cements

2.2.1. Particle size distribution and morphology of the starting powders

The particle size distribution was measured by laser diffraction using a Mastersizer 3000 (Malvern Panalytical, Kassel, Germany) applying the Mie scattering model. Isopropanol was used as dispersing medium, and stirring was performed with a speed of 3,000 U/min. The powders were deagglomerated with ultrasound for 1 min before measurements. Each powder was independently prepared 3 times, while 10 measurement runs were performed per preparation.

The morphology of the particles was monitored using a scanning electron microscope (SEM) Crossbeam 340 (Zeiss, Oberkochen, Germany) with an acceleration voltage of 2 kV. For that, the β-TCP raw powders were suspended in 2-propanol, transferred to a sample holder and left to dry overnight. Then, they were coated with a 4 nm platinum layer in an ACE600 (Leica, Wetzlar, Germany) sputter coating unit.

2.2.2. X-ray diffraction and structural analysis by Rietveld refinement method

The X-ray diffraction (XRD) analyses of the powders were performed with a diffractometer D8 (Bruker AXS, Karlsruhe, Germany) equipped with a nine-fold sample changer and Cu K_α radiation, produced at 40 kV and 40 mA. Data sets were collected in the 2θ range of 10–70°, with a step size of 0.0112° and an integration time of 0.4 s.

For the in-situ XRD measurements, a diffractometer D8 Advance with DaVinci design (Bruker AXS, Karlsruhe, Germany) was applied. The cement pastes with 0.75 wt% IP6 were prepared into special sample holders and covered with Polyimide Kapton film (Chemplex Industries, Palm City, FL, USA). Data sets were collected in the 2θ range of 6–39°,

step size of 0.0122°, and integration time of 0.075 s, at 37 °C. The generator settings were the same as for the powder measurements. XRD measurements for all powders and cements were repeated three times with three independent samples.

The quantitative phase composition was determined using Rietveld refinement with TOPAS 5.0 (Bruker AXS, Karlsruhe, Germany) combined with the G-factor method, an external standard method [31]. More details about this method applied for CPCs are well reported [13, 32]. β-TCP was refined with structure data set ICSD #97500 [23]. In the powder measurements, refined parameters were scale factor, lattice parameters, crystallite size (Lorentz contribution), and microstrain (Gauss contribution), together with the background as Chebyshev polynomial of the fifth order. Occupancies of Li^+ and Ca^{2+} were refined on the Ca(4) position, assuming a substitution mechanism of $Ca^{2+} \leftrightarrow 2$ Li^+. Since the scattering factor of P^{5+} is not included in the TOPAS software, Si^{4+} with a nearly identical scattering factor was inserted instead [22].

Lattice parameters, occupancies, and microstrain of β-TCP obtained from powder refinement were fixed for the *in-situ* XRD evaluation. In addition, structure data set ICSD #16132 [33] was applied for brushite, ICSD #917 [34] for monetite and ICSD #133 [35] for MCPM. Scale factors, lattice parameters, crystallite size (Lorentz contribution), and microstrain (Gauss contribution) were refined for the hydrate phases and constrained to reasonable values. Additionally, preferred orientations were added where necessary. The background contributions of water and the Kapton film were each refined by hkl models [36].

2.2.3. ^1H nuclear magnetic resonance (^1H NMR) of the cements

^1H NMR measurements were conducted at a Bruker minispec mq20 operating at 19.95 MHz, equipped with a temperature-controlled probe head. A combined solid echo (SE) - CPMG sequence was applied to determine relaxation times T_2, with a limit of 0.09 ms for the SE signal. Evaluation of the data was performed with the MinErSys framework based on the Contin software [37]. For *in-situ* ^1H NMR measurements of setting cement pastes, the temperature was adjusted at 37 °C, and one measurement run was performed every 5 min. Each composition was measured three times.

2.2.4. Preparation of storage samples

Storage samples of cements with 0.75 wt% IP6 were fabricated to enable detailed XRD characterization (quantities, lattice parameters, crystallite size, microstrain) of the hydrate phases after completion of hydration and to facilitate direct comparison of XRD and ^1H NMR quantification results. For this, cement pastes were filled into special plastic containers (inner diameter 23 mm; inner height 3 mm), the containers were sealed with Parafilm. Samples were stored in an incubator Heratherm (Thermo Fisher Scientific, Schwerte, Germany) at 37 °C. After 24 h, the samples were ground with an agate mortar and pestle to exclude any surface effects which might occur directly under the lid. The powders were then quantitatively analyzed by XRD and ^1H NMR, with the identical sample being used for both methods to ensure direct comparability of the resulting quantities.

2.2.5. Isothermal calorimetry

The heat flow evolved during cement hydration was measured with a TAM Air isothermal calorimeter (TA Instruments, New Castle, DE, USA) equipped with eight measurement channels in twin type arrangement. The mixture of the cement pastes was performed in special tools for internal stirring (InMixEr - **In**jection & **Mix**ing device for internal paste preparation, FAU **Er**langen, Mineralogy) using an external motor with a defined, constant stirring rate of 858 rpm, thus providing reliable data for the initial heat flow. Measurements were performed at 15 °C and 37 °C, and each measurement was reproduced three times. The evaluation was performed with Microcal Origin V 2019. The heat flow curves were corrected for the calibration constant of the InMixEr tools and the time constant [38].

2.2.6. Pore water analysis and ion release measurement

The pore solution of cements prepared with 3 wt% IP6 was extracted to determine the ionic concentrations. Based on the results of isothermal calorimetry, appropriate time points before the onset of the main reaction were selected at 2 h and 3 h, respectively, for Li5–BrC and BrC samples, and at 24 h for the fully reacted samples. The cement pastes were hardened in sealed containers in the Heratherm incubator at 37 °C. After 2 or 3 h, the pore water was extracted by centrifugation at 4,000 rpm for 8 min in a centrifuge Megafuge 1.0 (Heraeus Instruments, Hanau, Germany). The supernatant liquid was filled into a syringe and injected through a 0.45 mm sieve to remove residual particles. After 24 h, the pore water was extracted with a hydraulic press Metallkraft WPP 30 (Stürmer, Hallstadt, Germany) with an extraction cell (REMT Industrie, Grenay, France). To stabilize the solution, the pore water (1 ml) was mixed with 0.5 ml of diluted HNO_3 (1:1). The relevant elements' concentration was measured using an iCAP Qc inductively coupled plasma spectroscopy (ICP-MS) (Thermo Scientific, Waltham, MA, USA), and the operating conditions are given in supplementary information (Table S1, Supplementary Material). Before mixing with HNO_3, the pH of the pore water was recorded using a SevenCompact S220-Uni (Mettler-Toledo, Gießen, Germany).

Li^+ and Ca^{2+} release from Li5–BrC samples with dimensions of 6x6x12 mm^3, prepared with 3 wt% IP6, was evaluated by immersing them in 30 ml of phosphate-buffered saline (PBS) (130 mM NaCl, 7 mM Na_2HPO_4, 3 mM NaH_2PO_4) for 1 and 7 d at 37 °C. For this purpose, the paste was allowed to harden for 1 d at 37 °C prior to immersion. After each time point, 1.5 ml of PBS was collected and analyzed by ICP-MS. Three measurements were reproduced independently.

2.2.7. Initial and final setting times of the cements

The hardening performance of the cements was analyzed with an IMETER (IMETER/MSB Breitwieser MessSysteme, Augsburg, Germany) using the "Auto-Gilmore-Needle" approach. The IMETER method Nr. 20 was applied, providing H_{i20} data as a measure for the cement hardness [39]. A cylindrical indenter with a defined weight of 213.3 g and a needle diameter of 0.692 mm was applied. The cement sample prepared into a circular sample holder was lifted against this indenter during measurement, resulting in hardness-dependent load relief. The initial (IST) and final setting times (FST) of the brushite cements were automatically determined according to the definitions for biocements (IST: H_{i20} = 3.94 MPa/mm; FST: H_{i20} = 63.0 MPa/mm). The sample holder was automatically moved stepwise after each measurement to ensure that an intact spot was available for each following measurement. A break time of 20 s between measurement points was chosen. The temperature in the sample chamber was adjusted at 37 °C.

2.2.8. Compressive mechanical strength

The compressive strength (CS) of the set cements, prepared with 0.75 wt% IP6, was determined in a universal testing machine Z010 (ZwickRoell GmbH & Co. KG, Ulm, Germany), after their storage in rectangular-shaped silicon molds (6x6x12 mm^3) at 37 °C and 100% humidity for 1 d. The samples were loaded to failure at a crosshead speed of 30 mm/min at room temperature. The final CS in MPa was then calculated by setting the maximum force [N] in relation to the area. The microstructure of the fractured cements was observed by SEM. At least 12 samples were tested.

2.3. In vitro characterization of the cements

2.3.1. Human adipose-derived stem cell (hASCs) isolation and culture

Human adipose-derived stem cells (hASCs) were obtained from human adipose tissue after the liposuction procedure, performed at Hospital da Prelada (Porto), after the patient's informed consent, and under a collaboration protocol approved by the ethical committees of both institutions. To isolate the hASCs, the adipose tissue was submitted to 0.05% collagenase type II (Sigma) action under agitation for 1 h at

37 °C. Then, it was centrifuged at 800 rpm for 10 min, resuspended in phosphate buffer saline (PBS, Sigma Aldrich), again centrifuged at 350 rpm for 5 min, and finally resuspended in Minimum Essential Media α (α-MEM, Gibco), supplemented with 10% fetal bovine serum (FBS, Invitrogen), and 1% antibiotic/antimycotic (AB, Invitrogen). The cultures were maintained at 37 °C under a humidified atmosphere of 5% v/v CO$_2$ in air. The hASCs were selected by plastic adherence and passage at 80% confluence, and cells in passage 5 were used.

Cell proliferation and differentiation effect on the cements were evaluated on BrC and Li5–BrC samples, prepared with 3 wt% IP6. For that, the cells were seeded at a density of 2,500 cells/cm^2 in 24-well plates. For the relative gene expression analysis, cells were seeded at the same density in 6-well plates. After 24 h, the cell culture medium was substituted by 1 mg/mL of powdered cements milled up to an average particle size of about 15 μm in standard cell culture medium (α-MEM supplemented with 10% FBS and 1% AB), hereafter designated BM, or osteogenic culture medium (α-MEM supplemented with 10% FBS, 1% AB, 100 nM dexamethasone (Sigma Aldrich), 10 mM β-Glycerophosphate (Sigma Aldrich) and 0.05 mM of ascorbic acid (Wako)), hereafter designated OM. This range of cement concentration was chosen, as 1 mg/ml already resulted in a saturated solution [40]. Both suspensions were prepared and incubated at 37 °C for 24 h before the medium change. Of note, the cements were sterilized by γ-radiation before testing them in cell cultures. Cell cultures without powders were used as control (CTRL). Cultures were kept for 21 d at 37 °C under a humidified atmosphere of 5% v/v CO$_2$ in air. On days 1, 7, 14, and 21 of culture, cells' metabolic activity, proliferation, alkaline phosphatase (ALP) activity, collagen content, and relative gene expression were analyzed.

2.3.2. Metabolic activity and proliferation of hASCs cultured in the cements

Cells' metabolic activity was assessed using Alamar Blue reagent (ALAMAR BLUE®, AbD, UK). At each time-point, cells were rinsed with PBS and incubated with 10% v/v of Alamar in α-MEM culture medium for 3 h at 37 °C with 5% CO$_2$ and protected from light. Afterward, 100 μL of supernatant was transferred from each well in triplicate to a new 96-well tissue culture polystyrene plate. Fluorescence intensity was read at 530/20 nm (excitation) and 590/35 nm (emission) using a microplate reader (Synergy HT, Bio-Tek, USA). Alamar Blue in the medium was used as a blank.

To quantify cell proliferation, total double-stranded DNA (dsDNA) was assessed. First, at each time point, the cells were lysed by incubating them for 1 h at 37 °C in ultrapure water followed by storage at −80 °C. Then, the cells in ultrapure water were thawed and sonicated for 5 min. This cell lysate was used for dsDNA quantification using the Quant-iT PicoGreen dsDNA kit (Molecular Probes, Invitrogen), according to the manufacturer's instructions. RFUs were converted into ng/ml using a standard curve of DNA in the range of 1–2 μg/ml.

2.3.3. Alkaline phosphatase (ALP) activity

To quantify ALP activity, cell lysate previously produced was used. For that, 80 μl of cell lysate were combined with 20 μl of 1.5 M of Alkaline buffer solution (Sigma-Aldrich) and 100 μl of 4 mg/ml of phosphatase substrate (Sigma-Aldrich, USA). Then samples were incubated in the dark for 1 h at 37 °C. At this point, the reaction was stopped by adding 100 μl of 0.3 M of NaOH (PanReac AppliChem), and the absorbance was read at 405 nm using a microplate reader. The ALP activity was determined using a standard curve obtained from different dilutions of 4-Nitrophenol (Sigma-Aldrich) solution 10 mM, ranging from 0 to 250 μM.

ALP activity was also assayed by cytochemistry. For that, cell layers were fixed with 10% Neutral Buffered Formalin (ThermoFisher Scientific) for 20 min and permeabilized for 5 min with 0.1% v/v Triton X-100 (Sigma-Aldrich) in PBS. Afterward, cells were incubated for 30 min in Naphthol AS-MX phosphate/Fast Violet B salt (Sigma) at 37 °C and in the dark. Finally, hASCs were washed in PBS and observed using a microscope (Leica DM750).

2.3.4. Collagen expression

To investigate collagen expression, Sirius Red/Fast Green Collagen Staining Kit was used according to the manufacturer's instruction. Stained cells were first observed at the microscope, and then dye was extracted for collagen content quantification. Absorbance (Abs) values were transformed into μg/section using the following Eq. (3):

$$\text{Collagen } (\mu g/\text{section}) = \frac{Abs\ 540\ value - (Abs\ 605\ value \times 0.291)}{0.0378}$$

(3)

2.3.5. RNA isolation and real-time quantitative Reverse Transcriptase-Polymerase Chain reaction (qRT-PCR)

The mRNA levels for the genes of interest to evaluate the effect of Li5–BrC on hASCs were measured by real-time PCR analysis. After 14 and 21 days of culture, cells were detached from culture plates, immersed in TRI Reagent®, and stored at −80 °C until analysis. Total RNA was extracted from cells using the Direct-zol™ RNA MiniPrep kit (Zymo Research, Irvine, CA, USA), following the manufacturer's instructions. RNA quantification was assessed using a Nano-Drop ND-1000 spectrophotometer (Nano-Drop Technologies, Wilmington, DE, USA). The first-strand complementary DNA (cDNA) synthesis was performed according to the protocol from qScriptTM cDNA synthesis Kit (Quanta Biosciences, Gaithersburg, MD, USA) in a MiniOpticon real-time PCR detection system (BioRad, Hercules, CA, USA), using 500 ng of the total RNA from samples to generate single-stranded cDNA by random priming with qScript Reverse Transcriptase (RT). The obtained cDNA was then used as a template for amplifying the genes of interest (primers in Table S2, Supplementary Material) using the PerfeCta SYBR Green FastMix kit (Quanta Biosciences, Gaithersberg, MD, USA) according to the manufacturer's instructions. The endogenous housekeeping gene glyceraldehyde 3-phosphate dehydrogenase (GADPH) was used to normalize the transcripts expression data, and the relative gene expression quantification was calculated using as a calibrator the expression levels of hASCs collected at the time of cell seeding (day 0), according to the Livak (2$^{-\Delta\Delta CT}$) method.

2.3.6. Immunodetection of bone-specific proteins

Immunocytochemistry analysis was performed to detect Col I: using a rabbit anti-human polyclonal antibody against Col I (Abcam, Cambridge, UK; dilution 1:100); OCN: using a mouse anti-human monoclonal antibody against OCN (clone OC4-30, Abcam, Cambridge, UK; dilution 1:25); OPN: using a rabbit anti-human polyclonal antibody against OPN (Abcam, Cambridge, UK; 1:50). Cells were washed with PBS, fixed for 10 min at RT in 10% (v/v) formalin (ThermoFisher Scientific, Waltham, MA, USA), and stored at 4 °C until further use. Afterward, all samples were permeabilized with 1% (v/v) Triton X-100 (Sigma-Aldrich, St. Louis, MO, USA)/PBS for 10 min and blocked with 3% (w/v) bovine serum albumin (BSA; Sigma-Aldrich, St. Louis, MO, USA)/PBS solution for 45 min at RT. Samples were incubated with the primary antibodies overnight at 4 °C, prepared in 1% (w/v) BSA/PBS solution, and then with the respective secondary fluorochrome-conjugated antibodies: anti-rabbit/mouse IgG (ThermoFisher Scientific, Waltham, MA, USA; dilution 1:100) 2 h at RT, in the dark. Finally, nuclei were stained with 4′,6-diamidino-2-phenylindole (DAPI; Biotium, San Francisco, CA, USA; dilution 1:500) solution for 30 min at RT. Samples were observed under a Leica TCS SP8 confocal laser scanning microscope.

2.4. Statistical analysis

Statistical analyses for the biological tests were performed using GraphPad Prism 7.0 software (GraphPad Software, La Jolla, CA, USA). To evaluate differences for metabolic activity, proliferation, ALP
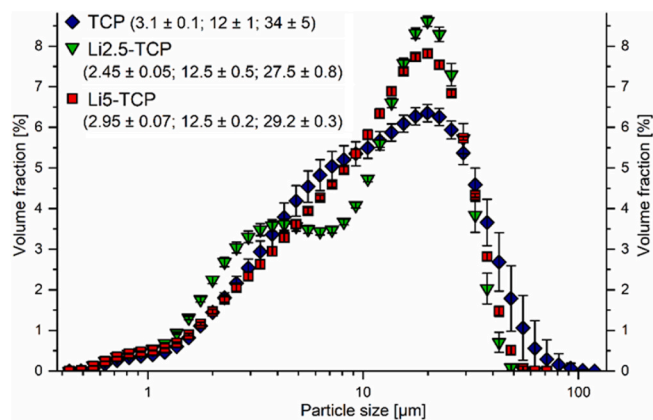
Fig. 1. Particle size distribution of TCP, Li2.5-TCP, and Li5-TCP powders determined by laser diffraction analysis. Results are the mean ± SD of 3 independent experiments. D_V10, D_V50, and D_V90 values in μm are given in brackets.

activity, and collagen expression results, a non-parametric Kruskal-Wallis test followed by Dunn's test for multiple comparisons was used. The results from real-time PCR analysis were analyzed by means of a Mann-Whitney test. Shapiro-Wilk normality test was performed to ascertain data normality. The significance level was set to *p < 0.05, **p < 0.01, ***p < 0.001, ****p < 0.0001. For the physicochemical characterization of the powders and cements, data are presented as mean ± standard deviation (SD).

3. Results and discussion

3.1. Li$^+$ -doped β-TCP powders

The particle size distributions of the powders with different Li$^+$ content slightly differed, but were still in a comparable range (Fig. 1). The content of larger particles above around 30 μm was higher in TCP, compared to the Li$^+$-containing samples. Li2.5-TCP showed a more bimodal particle size distribution, while the particle sizes where continuously spread over a broad range of grain sizes in TCP and Li5-TCP. The SEM images (Fig. S1, Supplementary Material) confirmed this broad particle size distribution, as very small grains with diameters far below 1 μm were accompanied by large grains. The size of the large particles in TCP was higher than in both Li$^+$ containing samples, as indicated by laser diffraction. While the grains in both Li2.5-TCP and Li5-TCP had sharper edges, those in TCP were more rounded.

The quantification by G-factor method resulted in β-TCP contents of 97.5 ± 0.8 wt% for TCP, 92 ± 2 wt% for Li2.5-TCP, and 94.6 ± 0.7 wt% for Li5-TCP, and no crystalline secondary phases were detected. This confirmed that if at all, only minor amounts of amorphous phase were present. The lattice parameter a decreased with increasing Li$^+$ content, while the c parameter increased for Li2.5-TCP, followed by a decrease (Fig. 2 A). The unit cell volume linearly decreased with increasing Li$^+$ content (Fig. 2 B). The Li$^+$ content incorporated in β-TCP was determined from the Li$^+$ occupancies on the Ca(4) position. This resulted in 2.1 ± 0.1 mol% Li$^+$ for Li2.5-TCP and 4.6 ± 0.2 mol% Li$^+$ for Li5-TCP. Hence, the refined values were close to the theoretically expected ones.

Both developments of unit cell volume and occupancies confirm the successful incorporation of Li$^+$ into the structure of β-TCP on the Ca(4) position. The decrease of the unit cell volume with increasing Li$^+$ incorporation is in accordance with the literature [41–43]. It can be explained by the ionic radii, which are 1.00 Å for Ca^{2+} and 0.76 Å for Li$^+$ (both for 6-fold coordination) [44]. There is general agreement about the decrease of the *a* parameter by Li$^+$ addition [25,41,42]. The present study also confirmed this, but some reports slightly differ about the development of the *c* parameter: No variation was detected in Ref. [41], while other studies observed an increase [42] or a slight decrease [25]. Therefore, the effect on the *c* parameter is not unambiguous. However, the unit cell volume development can be taken as reliable proof for Li$^+$ incorporation. Since no secondary phases were detected, the proposed substitution Ca^{2+} ↔ 2 Li$^+$ mechanism is also confirmed.

3.2. Brushite cements incorporating Li$^+$

3.2.1. Characterization of the hydration products and setting reaction

3.2.1.1. Storage samples. All cements prepared with 0.75 wt% IP6 and hardened at 37 °C for 24 h were composed of brushite, monetite, and minor amounts of residual β-TCP (Table S3, Supplementary Material), and no systematic trend was observed for different Li$^+$ contents. No significant variation of the lattice parameters with changing Li$^+$ content was noticed for both brushite and monetite (Table 1). Their crystallite sizes and microstrains were comparable between the samples (Table S4,

Table 1
Lattice parameters of the storage samples prepared with 0.75 wt% IP6 and hardened at 37 °C for 24 h.

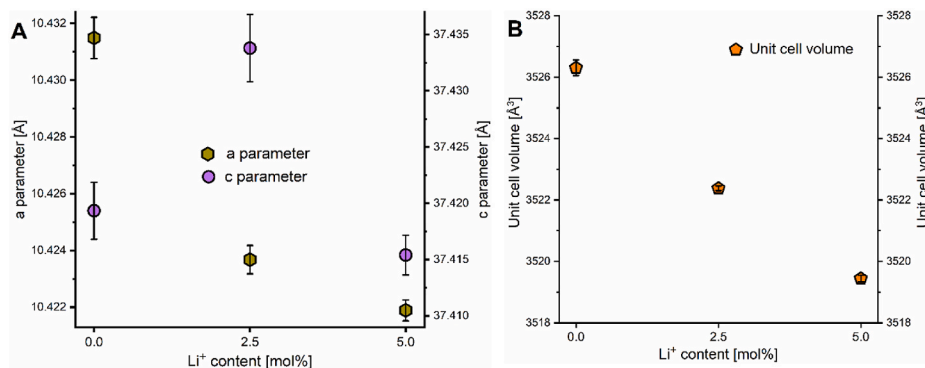| Sample	Brushite			Monetite		
	a [Å]	b [Å]	c [Å]	a [Å]	b [Å]	c [Å]
BrC	5.8179 ± 0.0002	15.199 ± 0.001	6.2499 ± 0.0002	6.9079 ± 0.0007	6.6408 ± 0.0004	6.9999 ± 0.0003
Li2.5-BrC	5.8190 ± 0.0010	15.199 ± 0.002	6.2504 ± 0.0008	6.9088 ± 0.0011	6.6422 ± 0.0012	7.0011 ± 0.0015
Li5–BrC	5.8183 ± 0.0008	15.200 ± 0.002	6.2503 ± 0.0012	6.9101 ± 0.0012	6.6399 ± 0.0017	6.9991 ± 0.0022

Fig. 2. Development of **A)** lattice parameters a and c, and **B)** unit cell volume of β-TCP with different Li$^+$ contents. Results are the mean ± SD of 3 independent experiments.
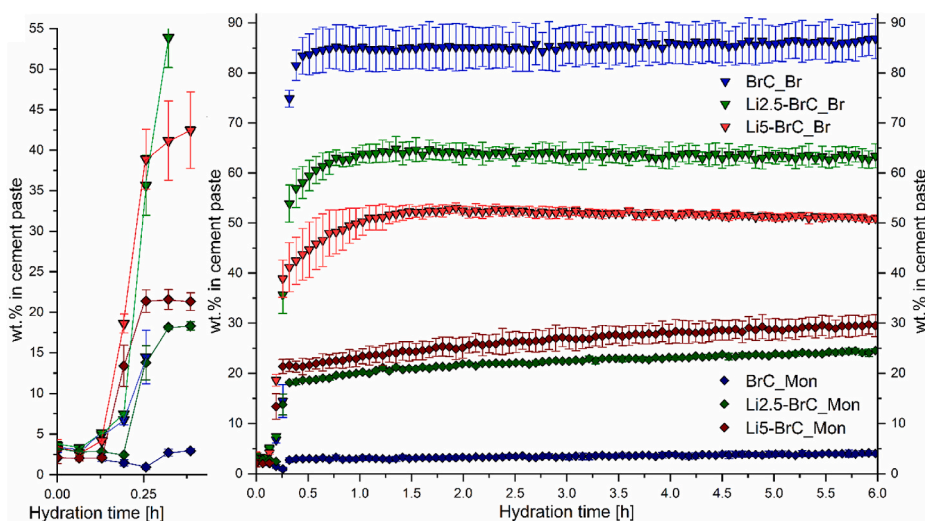
Fig. 3. Quantitative *in-situ* XRD results of BrC, Li2.5-BrC, and Li5–BrC, obtained with 0.75 wt% IP6, measured at 37 °C. Mon: monetite; Br: brushite. Results are the mean ± SD of 3 independent experiments.

Supplementary Material). Hence, there is no hint of Li$^+$ incorporation into brushite or monetite.

The identical storage samples were further analyzed by ^{1}H NMR. They all contained three different proton reservoirs, distinguishable by their different relaxation times T_2 (see the exemplary plot of Li5–BrC in S2 A, Supplementary Material). After quantification of these proton reservoirs, the brushite, monetite, and water quantities were derived. It was assumed that the rigid fraction (lowest T_2) constituted the protons in brushite, the intermediate fraction those in monetite, and the mobile one (highest T_2) the residual H_2O, as samples with higher XRD monetite quantities systematically exhibited more elevated amounts of intermediate fraction and vice versa. The intermediate signal was located at around $T_2 = 0.05$ ms, being part of the SE signal with an upper limit of $T_2 = 0.09$ ms. It has to be considered that the samples might additionally contain an amorphous solid fraction, as the wt% of amorphous fraction obtained from G-factor (which includes residual H_2O) was higher than the theoretical amount of residual water (Table S3, Supplementary Material). As no additional signal was detected by ^{1}H NMR and there was no systematic overestimation of the brushite/monetite wt ratio by one of the methods, the protons of the proposed amorphous hydrate phases were assumed to be equally included in the signals of both crystalline brushite and monetite.

The wt ratios of brushite/monetite calculated by this method were compared to those obtained from XRD quantification. While the data were not identical, the trend was still clearly comparable (Table S5, Supplementary Material). Hence, assuming that both data have some error, it is likely that the assignation of the proton reservoirs is correct. This was further confirmed by three additional samples (all measured as powders with the addition of a few droplets of water to ensure comparability): In BrC stored at 23 °C for 24 h, containing 88 wt% of brushite (Fig. S2 B, Supplementary Material), only the rigid signal at T_2 around 0.01 ms was visible. Pure monetite (CaHPO$_4$ from Alfa Aesar) revealed only the intermediate signal (Fig. S5 C, Supplementary Material). In a 3:2 w/w mixture of these two materials (Fig. S2 D, Supplementary Material), both signals were visible, and quantification, as described above, resulted in a brushite/monetite wt% ratio of 1.15 ± 0.06. For comparison, the theoretical ratio would be 1.3, taking into account the brushite contents of the storage samples.

These observations demonstrate that T_2 of brushite is significantly lower than T_2 of monetite. The protons in the brushite structure must hence be less mobile and more tightly bound than in the monetite structure.

3.2.1.2. In-situ XRD. The evolution of crystalline phases in cements with 0.75 wt% IP6 was obtained through *in-situ* XRD measurements. Formation of brushite and monetite was observed, with brushite as the major phase (Fig. 3). While minor amounts of both phases were already detectable from the beginning, rapid precipitation of higher quantities started after few minutes, with brushite increase starting earlier. This rapid precipitation was accompanied by a rapid β-TCP dissolution in all samples (Fig. S3, Supplementary Material). The brushite content decreased with increasing Li$^+$ content, and accordingly, the monetite content increased, with the most pronounced difference between BrC and both Li$^+$ containing cements (Fig. 3). In the Li$^+$ containing cements, the monetite content slightly continued to increase after completion of β-TCP dissolution and brushite formation (from 20.9 ± 0.2 to 24.5 ± 0.3 wt% for Li2.5-BrC; and from 24 ± 2 to 30 ± 2 wt% for Li2.5-BrC). It appeared that in these two samples the brushite content slightly decreased at the same time. However, this was not significant.

3.2.1.3. In-situ ^{1}H NMR. The *in-situ* ^{1}H NMR data of the cements were evaluated according to the procedure developed with the storage samples; the raw data for the proton quantification are presented in Fig. S4 and the corresponding level plots in Fig. S5 (Supplementary Material). The quantities obtained (Fig. 4) confirmed the observations implied by *in-situ* XRD: After completion of the hydration, the brushite content decreased over time, while the monetite content increased. This was further indicated by an increase of the mobile proton fraction (H_2O) over time in the *in-situ* ^{1}H NMR raw data. As *in-situ* ^{1}H NMR analyzed the bulk sample, it was proven that this effect was not limited to the sample surface. Hence, after completion of hydration, brushite started to dehydrate, according to Eq. (4).

$$CaHPO_4 \cdot 2H_2O \rightarrow CaHPO_4 + 2H_2O \qquad (4)$$

Dehydration of brushite is reported to be completed at temperatures around 200-220 °C, while slow dehydration can already occur at lower temperatures with prolonged exposure to heat [45], and indications for a transformation of brushite to monetite during cement setting for specific cement compositions were described [11]. Since monetite is thermodynamically more stable according to thermodynamic calculations with the software GEMS (Gibbs Energy Minimization Software for Geochemical Modelling, Paul-Scherrer-Institut, Villigen, Schweiz) for the pure system without IP6, it is plausible that the composition developed towards higher monetite contents over time [46,47]. The effect was more pronounced for the Li$^+$ containing samples, suggesting that Li$^+$ accelerated the dehydration of brushite to monetite.
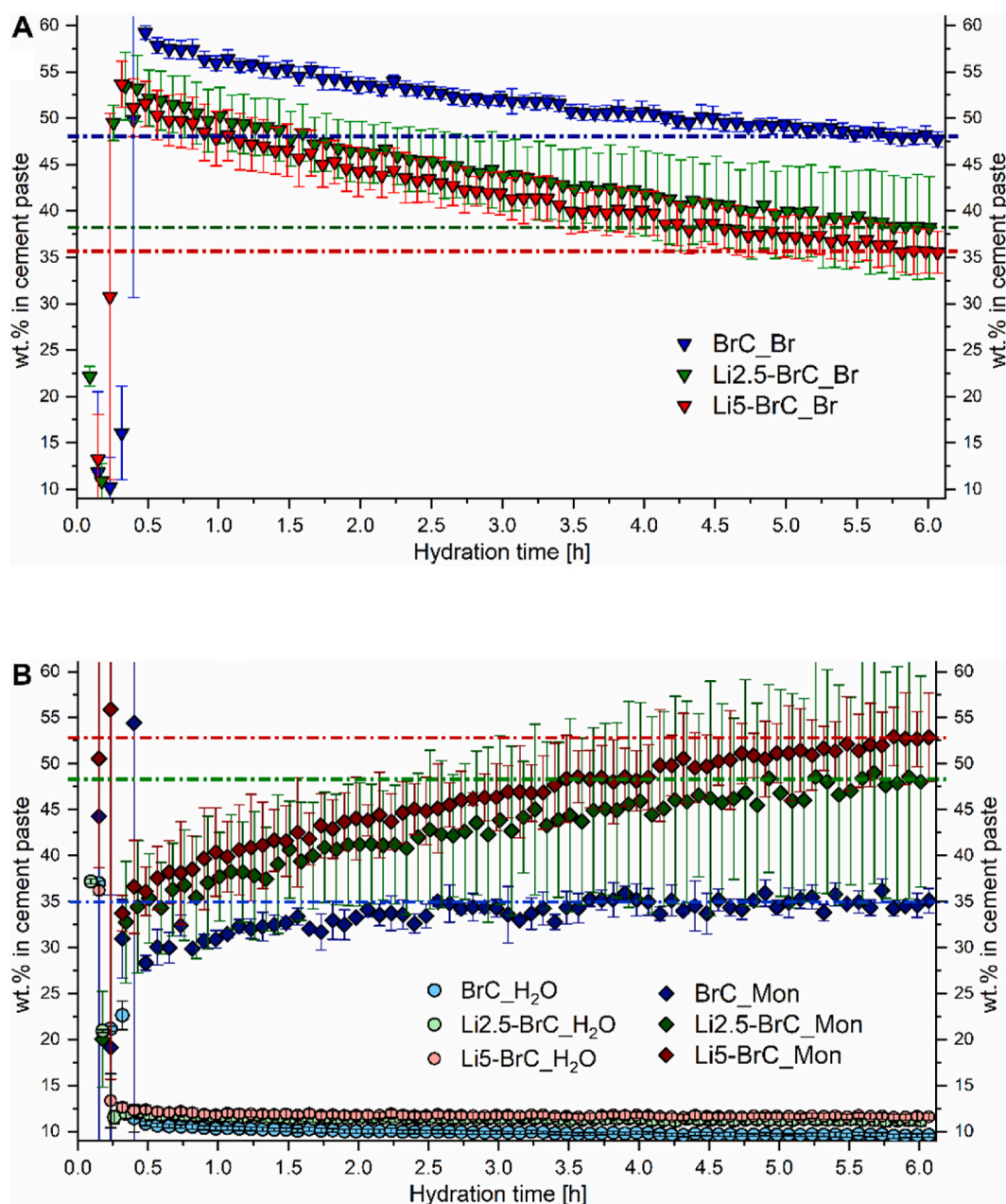
Fig. 4. *In-situ* ^{1}H NMR measurements of BrC, Li2.5-BrC, and Li5–BrC prepared with 0.75 wt% IP6, measured at 37 °C: **A)** Quantities of brushite, and **B)** Quantities of monetite and H_2O. Mon: monetite; Br: brushite. Results are the mean ± SD of 3 independent experiments.

The brushite content was generally high and the monetite content low in BrC, in accordance with *in-situ* XD results. Therefore, Li^+ seems to favor monetite formation already at the beginning. This might result from a destabilizing effect on brushite, or a stabilizing effect on monetite. However, since there were no signs for incorporation of Li^+ in these phases, this is not plausible, and other factors might be relevant.

It is further evident that the brushite/monetite wt% ratios obtained by *in-situ* ^{1}H NMR were lower than those from *in-situ* XRD for all samples investigated. This might result from the fact that *in-situ* ^{1}H NMR measures the bulk sample, while mainly the top 100-200 μm are analyzed by *in-situ* XRD. It is possible that brushite formation occurred preferably at the sample surface, resulting in the overestimation of brushite by *in-situ* XRD. Furthermore, the intense preferred orientation of the hydration products, especially brushite, can impair the accuracy of the *in-situ* XRD quantities. Hence, it appears that data obtained from *in-situ* ^{1}H NMR can be more reliable when bulk sample compositions are of interest or

hydrate phases tend to exhibit intense preferred orientation. However, it has to be considered that no distinction of crystalline and amorphous phases is possible by (*in-situ*) ^{1}H NMR, and the nature of crystalline phases cannot be identified. Hence, an intelligent combination of both methods is highly valuable to obtain reliable data.

3.2.1.4. Isothermal calorimetry. Isothermal calorimetry measurements of the cement pastes prepared with 0.75 wt% IP6 and measured at 37 °C showed a slight initial maximum, followed by a high, sharp main maximum (Fig. 5 A). The results show an accelerating effect of Li^+ with increasing concentration, observed by the positions of the main maxima at 15.7 ± 0.7 min for BrC, 13.9 ± 0.6 min for Li2.5-BrC, and 10.7 ± 0.7 min for Li5–BrC. The maximum dissolution rate increased, especially for Li5–BrC (546 ± 7 mW/g_{Solid} for BrC, 584 ± 2 mW/g_{Solid} for Li2.5-BrC, and 728 ± 67 mW/g_{Solid} for Li5–BrC).

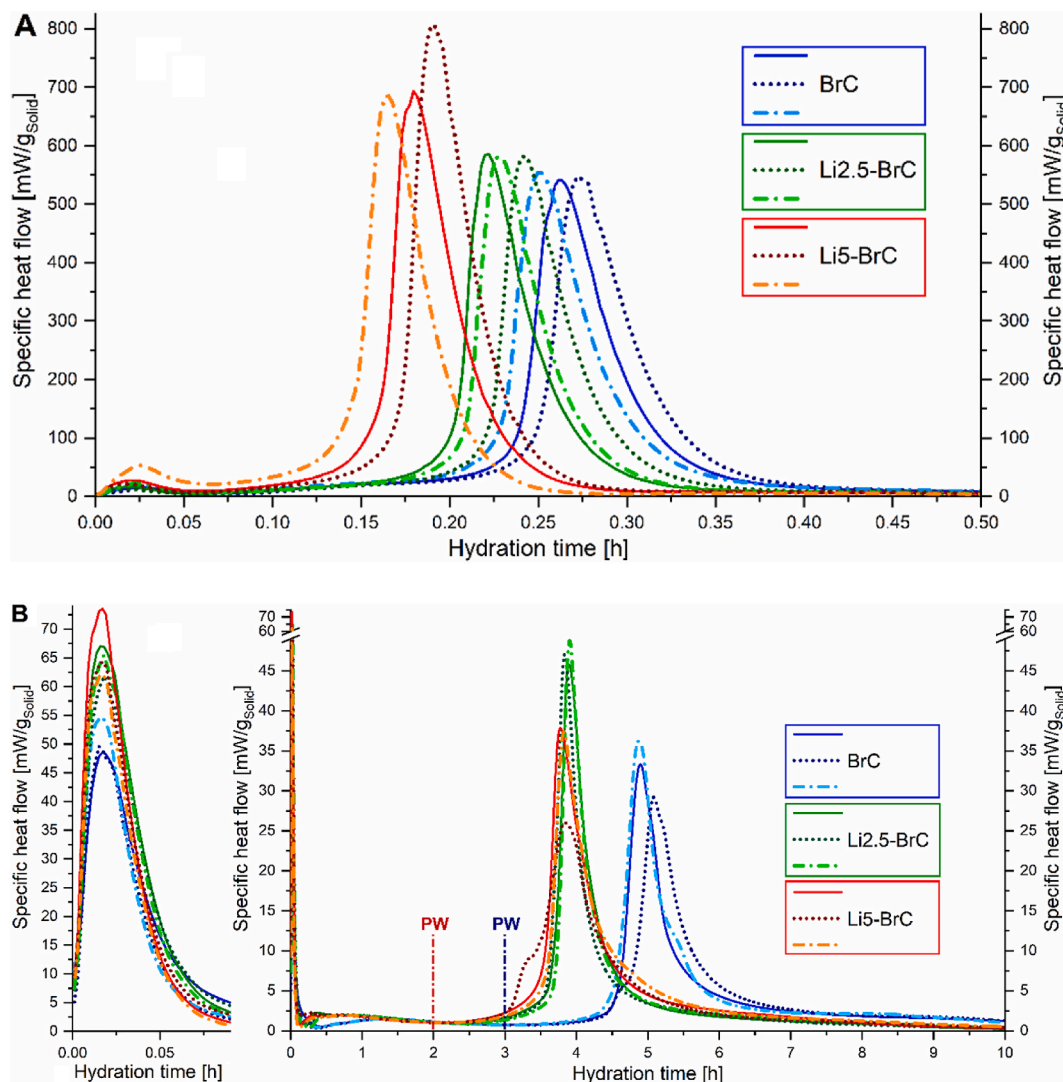The pastes prepared with 3 wt% IP6 and measured at 37 °C exhibited

Fig. 5. Isothermal calorimetry curves of the cement pastes at 37 °C prepared with **A)** 0.75 wt% IP6 and **B)** 3 wt% IP6. The results of all measurement runs are shown (n = 3).

an initial maximum and a sharp main maximum after a few hours (Fig. 5 B). A minor, broad maximum occurred in between. The reaction of both Li^+ doped samples was significantly accelerated, as both the main maximum and the broad maximum occurred earlier. However, no difference could be noted in the maximum position of Li2.5-BrC (3.88 ± 0.04 h) and Li5–BrC (3.81 ± 0.03 h). At 15 °C, the general trend of acceleration by Li^+ was confirmed, while the maxima of Li2.5-BrC (16.1 ± 0.7 h) were located in between those of BrC (19 ± 1 h) and Li5–BrC (12.6 ± 0.3 h) (Fig. S6, Supplementary Material).

Table 2
Element concentrations of the BrC and Li5–BrC in the pore water over time as determined by ICP-MS.

Sample	Element concentration [mmol/L]					pH
	Ca^{2+}	P	Li^+	C_{org}	Ca/P	
BrC_3h	2,430 ± 40	5,330 ± 10	n.d.	770 ± 30	0.46 ± 0.01	2.11 ± 0.01
BrC_24h	450 ± 200	1,200 ± 400	0.04 ± 0.01	120 ± 90	0.38 ± 0.08	3.0 ± 0.2
Li5–BrC_2h	2,320 ± 10	5810 ± 10	103 ± 1	818 ± 6	0.40 ± 0.01	2.03 ± 0.06
Li5–BrC_24h	330 ± 150	2,000 ± 200	750 ± 30	180 ± 120	0.2 ± 0.1	3.2 ± 0.1

Li^+ incorporated in the structure of β-TCP accelerated the hydration, while the general reaction mechanism of the cements was not altered. Since the particle size distribution was similar for all powders investigated, it is very likely that differences in reactivity do not just originate from different particle sizes. Theoretically, acceleration might result from possible destabilization of the β-TCP structure by Li^+ incorporation, increasing its solubility. However, current literature rather points that the transformation of Li-doped β-TCP to α-TCP was impaired [48, 49], which does not necessarily affect the solubility in solution but indicates a general stabilization of the structure. However, there were also studies directly showing reduced solubility of β-TCP in a saline solution (0.85% NaCl) by Li^+ doping [41]. Both effects were explained by the stabilization of the structure due to the full occupation of all Ca positions. Similar effects were described for incorporating smaller, divalent ions like Co^{2+} [50]. They are supposed to stabilize the structure due to their smaller ionic radii, resulting in an increased setting time of brushite cements fabricated from β-TCP and MCPM.

Actually, a pronounced increase in setting time was observed for several divalent ions [51], like Mg^{2+} [52], Zn^{2+} [15], Cu^{2+} [16] or Fe^{2+} [53], and for monovalent Ag^+ [54]. Contrary, there are only few reports about accelerating effects of ions substituting Ca^{2+} in β-TCP, as in the case of Co^{2+} that slightly decreased IST and FST when added in minor amounts (0.25 wt%), while 1 wt% of Co^{2+} increased both parameters.

The decrease for lower Co^{2+} amounts was attributed to the formation of the highly soluble $CoHPO_4$ [50]. An interesting observation was reported for Sr^{2+} doped brushite cement: While both IST and FST increased up to Sr^{2+} concentrations of 6.6 wt%, the setting times decreased again for higher concentrations (but were still above the values obtained for the reference). This reverse in trend was attributed to monetite formation, which was proposed to precipitate more rapidly than brushite [55]. Actually, the ratio of brushite/monetite detected at identical time points was lower in both Li^+ containing samples, as indicated by both *in-situ* XRD and *in-situ* ^{1}H NMR. However, there were no indications that monetite precipitation was generally more rapid in the cement system investigated here. Hence, this explanation is not really plausible.

3.2.1.5. Pore water analysis and ion release. The time points selected for pore water analysis before the onset of the main reaction of BrC and Li5–BrC prepared with 3 wt% IP6 are marked as "PW" in Fig. 5. Very high amounts of Ca^{2+} and P ions were measured (Table 2), which is expectable due to the rapid dissolution of the highly soluble MCPM [56]. Complete dissolution of MCPM would result in concentrations of about 4,500 mmol/L of Ca and 9,000 mmol/L of P, corresponding to a Ca/P ratio of 0.5.

The concentrations and the Ca/P ratio measured were significantly lower. This indicates the formation of an amorphous intermediate phase in addition to brushite and monetite, especially since presumably some β-TCP had been dissolved in addition. Concentrations of both ions clearly dropped after completion of the reaction after 24 h, hence the ions were consumed for precipitation of the hydration products. However, due to the poor reproducibility of these data, no reliable data for the actual values can be given.

Before the onset of the main reaction, 103 ± 1 mmol/L Li^+ were detected, which confirms that some dissolution of the Li^+ doped β-TCP has occurred. There are reports of priority dissolution of Li^+ compared to Ca^{2+} in a saline solution (0.85% NaCl) [41], which appears plausible due to the weak bonding at the Ca(4) position, where Li^+ is incorporated [23]. As pore water analysis proved the availability of Li^+ ions in solution before the start of the main reaction, the Li^+ might promote precipitation of the hydrate phases, possibly due to a decrease of brushite and monetite solubility by Li^+ incorporation. However, analysis of lattice parameters, crystallite sizes, and microstrain gave no hint of Li^+ incorporation into brushite or monetite (Table 1), contradicting this explanation.

To the best of our knowledge, there are no reports about the effect of Li^+ on the hydration of CPCs. However, Li^+ is known to remarkably accelerate the hydration of calcium aluminate cements even in minor amounts [57]. One theory for this is the rapid formation of a Li-containing hydrate phase, possibly acting as a nucleation substrate for the main hydration product [58]. Similar effects might occur in brushite cements. Parts of the Li^+ released from initial β-TCP dissolution might form a lithium phosphate hydrate phase. There were also indications for uptake of Ca^{2+} and P ions in an amorphous intermediate hydration product, since the initial concentrations of these ions were lower than expected. Hence, some X-ray amorphous lithium calcium phosphate hydrate might have formed as nucleation substrate.

The Li^+ content increased to a concentration of 750 ± 30 mmol/L during hydration, contrary to Ca^{2+} and P quantities development. Hence, a significant fraction of Li^+ was found in the pore solution after the completion of hydration. However, it is also possible that not all Li^+ was present in the solution. Parts of the ions might have been adsorbed on the hydrate phases or contained in solid lithium phosphates. Indeed, significant Li^+ release was observed in the leaching experiments in PBS at 37 °C. The concentrations of Li^+ and Ca^{2+} released from Li5–BrC cements were 3.8 ± 0.3 mmol/L Li^+ and 1.5 ± 0.1 mmol/L Ca^{2+} within 1 d, and 4.1 ± 0.1 mmol/L Li^+ and 1.6 ± 0.1 mmol/L Ca^{2+} within 7 d. With the experimental setup applied, release of all Li^+ incorporated in

Table 3

IST and FST of brushite cements prepared with 0.75 wt% IP6, determined at 37 °C by Imeter measurements.

Samples	IST [min]	FST [min]
BrC	20.3 ± 0.6	22.7 ± 0.5
Li2.5-BrC	16.4 ± 0.3	17.8 ± 0.7
Li5–BrC	13.4 ± 0.4	15.2 ± 0.7

the cement sample would result in a concentration of around 4.4 mmol/L. Hence, the major fraction of Li^+ was already released after 1 d, with only minor increase after 7 d.

The concentrations of C_{org}, resulting from IP6, clearly dropped from 2 or 3 h up to 24 h (Table 2). This confirms that at least the major part of IP6 was bound in a solid phase or adsorbed at particle surfaces afterward. If this were not the case, the measured concentration would increase, as the water uptake by brushite and monetite formation would result in an accumulation of the ions left in the pore solution.

The pH of the pore water increased during hydration. No significant differences between BrC and Li5–BrC with 3 wt% IP6 were observed (Table 2). Therefore, it is unlikely that variations in pH can explain the promotion of monetite formation by Li^+. Generally, monetite is favored by lower pH values [59]. Accordingly, a decrease of pH was presented as a possible explanation for Sr^{2+} promoting the formation of monetite, though no pH values were reported in that study [55]. The pH of BrC with 0.75 wt% IP6 was 2.5 immediately after mixing. Unfortunately, the value for Li5–BrC could not be obtained due to the fast initial thickening of the cement paste. However, since no difference was observed for 3 wt% IP6, it is plausible to assume that there is also no difference in pH for lower IP6 contents induced by Li^+ addition. Hence, it is likely that other aspects are responsible for the promoted monetite formation.

The %wt ratio brushite/monetite is supposed to affect cement degradation. Though the solubility of monetite under physiological conditions is lower than brushite [60], monetite shows faster resorption *in vivo*. This can be attributed to the transformation of brushite into hardly soluble hydroxyapatite [61]. Hence, brushite cements with higher monetite fraction degrade faster *in vivo*, and thus result in high Li^+ release. However, since at least a major part of Li^+ was proven to be present in the pore solution instead of a hydrate phase, a significant fraction of Li^+ might just diffuse out without degradation.

3.2.1.6. Initial and final setting times of the cements. In order to adjust the setting time for clinical needs, the IP6 concentration of the mixing liquid was varied for Li5–BrC (Fig. S7, Supplementary Material). Even a concentration of 1 wt% resulted in a rather slow hardening, with the IST and FST reached only after 29 ± 1 min and 35 ± 3 min, respectively. Reducing the IP6 amount to 0.75 wt%, resulted in significantly faster hardening. Both IST and FST clearly decreased with increasing Li^+ content for the cements prepared with 0.75 wt% IP6 (Table 3). For all samples, the difference between IST and FST was low, and the development of hardness was basically the same for all three samples, only shifted to earlier time points for higher Li^+ contents (Fig. S8, Supplementary Material).

In order to gain a deeper understanding of the cements hydration mechanism responsible for the hardening, the results of Li5–BrC prepared with 0.75 wt% IP6, obtained by *in-situ* XRD, isothermal calorimetry, and Imeter, were compared (Fig. S9, Supplementary Material). As expected, the sharp calorimetric maximum resulted from the rapid dissolution of β-TCP and immediate precipitation of brushite and monetite. The initial maximum was accompanied by a slight precipitation of brushite and monetite. The formation of these phases mainly runs parallel to the hardness development, which is as rapid as the brushite and monetite precipitation. This might explain why the IST and FST are so close together, *i.e.,* as soon as the hardening mechanism starts, it does not take much time for completion.
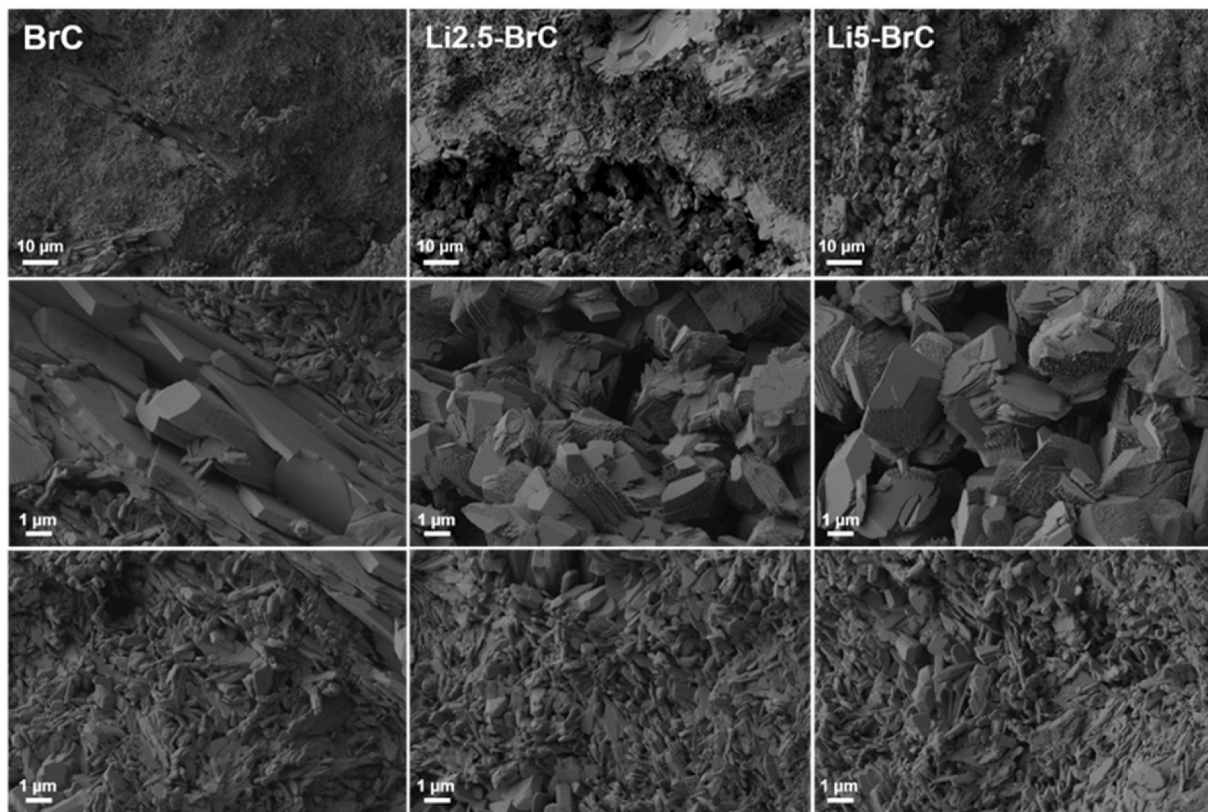
Fig. 6. SEM images of the cements prepared with 0.75 wt% IP6 and hardened for 24 h at 37 °C.
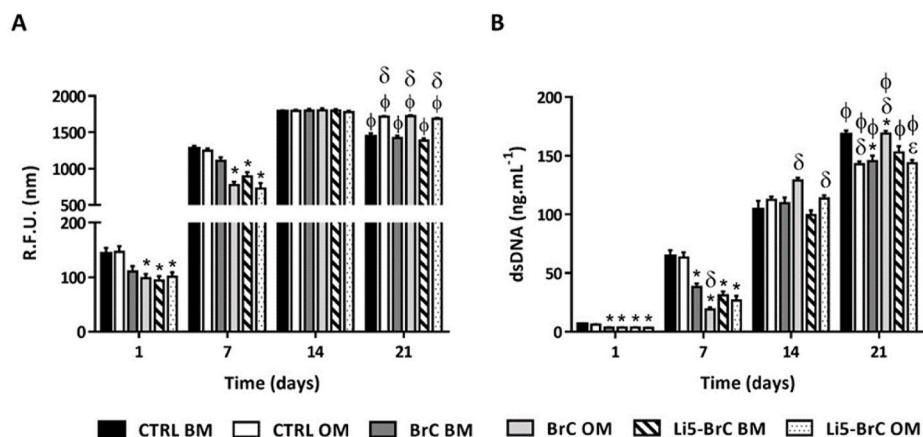

Fig. 7. *In vitro* assessment of the biological performance of BrC and Li5–BrC cement powders seeded with hASCs in different culture media (basal (BM) and osteogenic (OM) medium). **A)** hASCs metabolic activity; **B)** hASCs proliferation assessed by quantification of dsDNA. Symbols denote statistically differences when compared with CTRL (*), BM conditions (δ), and BrC (ε) at each time point and compared with day 1 (ϕ). Data are presented as mean ± SD (n = 3).

3.2.1.7. Compressive mechanical strength and microstructure of the set cements. The measured CS of the cements, after hardening at 37 °C for 1 d, achieved average values of 18 ± 3 MPa for BrC, 13 ± 3 MPa for Li2.5-BrC and 10 ± 2 MPa for Li5–BrC, with significant differences between all samples ($p < 0.05$). The results showed that the incorporation of Li^+ led to CS decreased in comparison to Li-free cements, probably due to the higher amount of monetite phase present in those samples, which can reduce the strength of set cements [62]. However, the values are in the range reported for brushite-forming cements, as well as within the range for trabecular bone (2-12 MPa) [51].

The morphological features of fractured surface of the cements are presented in Fig. 6. Tabular crystals typical for brushite and monetite can be observed, and no drastic changes on cement morphology were

induced by Li^+ incorporation [13,51,63].

3.2.2. In vitro evaluation of the Li-doped brushite cements

3.2.2.1. hASCs metabolic activity and proliferation. Cells' metabolic activity and proliferation were analyzed over culture in both cultured mediums to assess any deleterious effect of the developed cement powders (Fig. 7). The results showed that the cells were metabolically active (Fig. 7 A) and proliferative (Fig. 7 B) along the time of culture for all the tested conditions. Nevertheless, a decrease in metabolic activity and proliferation was observed at the first 7 days of culture for the cement powders compared with the CTRL. Such observation can
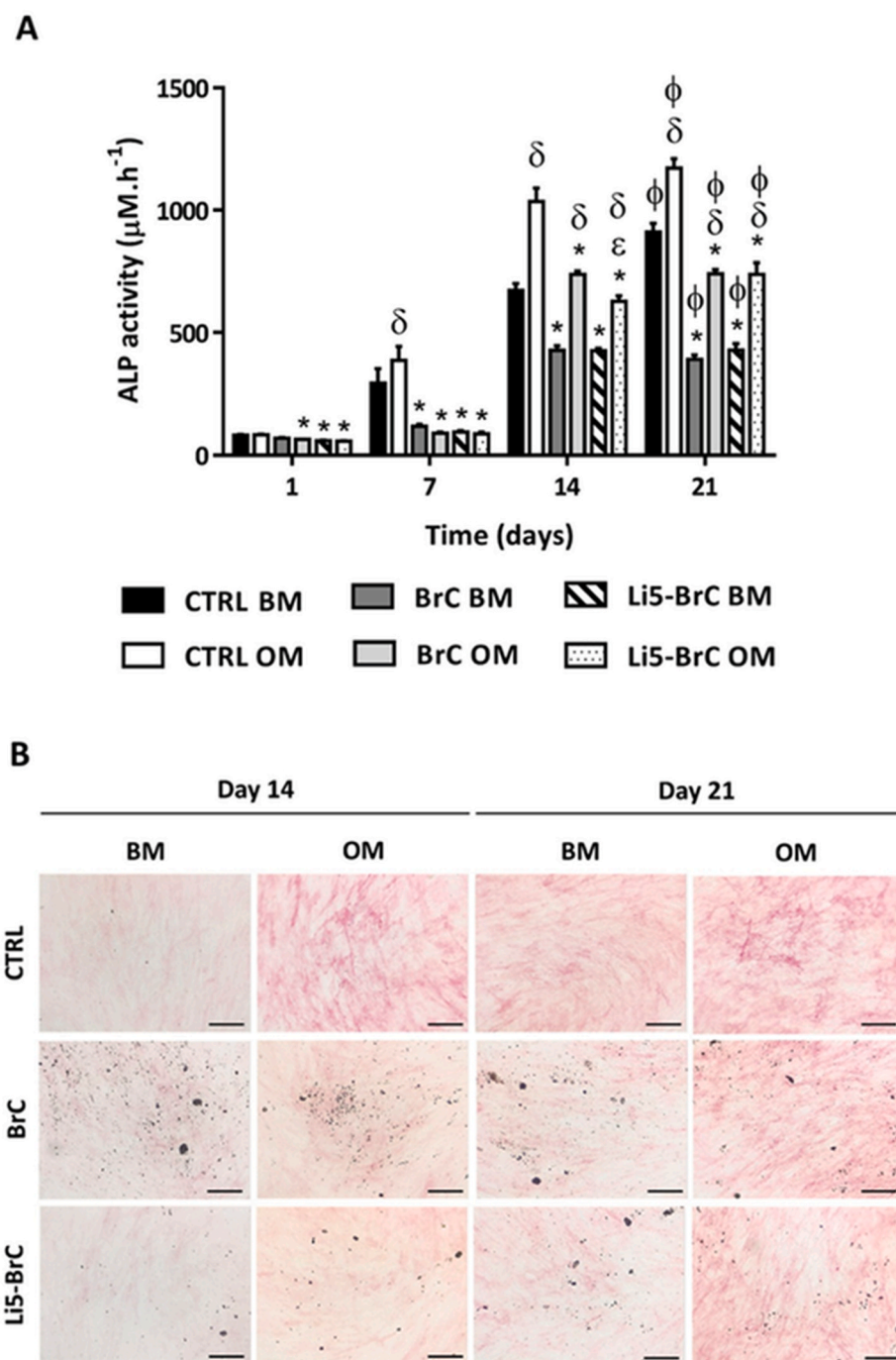
Fig. 8. *In vitro* evaluation of osteogenic differentiation in basal (BM) and osteogenic (OM) medium. **A)** Quantification of ALP activity; Symbols denotes statistically differences when compared with CTRL (*), BM conditions (δ), and BrC (ε) at each time point, and with day 1 and day 7 (ϕ). Data are presented as mean ± SD (n = 3). **B)** Staining of ALP expression (in red, scale bar = 200 μm). (For interpretation of the references to color in this figure legend, the reader is referred to the Web version of this article.)

correspond to the time of culture necessary for the cells to adapt to the cement powders' new environment. Indeed, on day 14, all conditions present similar values. These results indicate that the cement powders had no harmful effect, since the cells could recover to normal metabolic and proliferative levels. Finally, at day 21, a higher level of metabolic activity was observed for the OM conditions, compared to BM, and lower proliferation rates, indicating that cells in OM conditions were differentiated along the osteoblastic lineage. Noteworthy, despite BrC increasing metabolic activity in OM conditions at day 21, they were also more proliferative, thus indicating that it was not differentiating.

3.2.2.2. ALP activity and collagen expression. Since ALP is a well-known early marker of osteogenic differentiation, its activity was investigated to infer the effects of cement powders on the cells' differentiation

(Fig. 8). As previously observed, during the first 7 days, BrC and Li5–BrC showed lower ALP activity than CTRL conditions (Fig. 8 A). However, at day 14, despite being lower than the CTRL, ALP activity of BrC and Li5–BrC increased, showing higher values under OM conditions, as expected, and corroborated by the staining of ALP expression (Fig. 8 B). The same tendency was observed at day 21, with a more pronounced ALP expression under OM conditions (Fig. 8 B), indicating that the cement powders supported the cells' differentiation along the osteoblastic lineage and showing the positive effect of the presence of Li^+. The use of Li^+ in therapeutic strategies using stem cells was proven to have a significant role in regulating the proliferative activity and ability for differentiation and can improve the expression of late osteogenic markers in adipose-derived stem cells [64,65]. Additionally, Li^+ can lead to the accumulation of β-catenin in the cytoplasm, thus activating
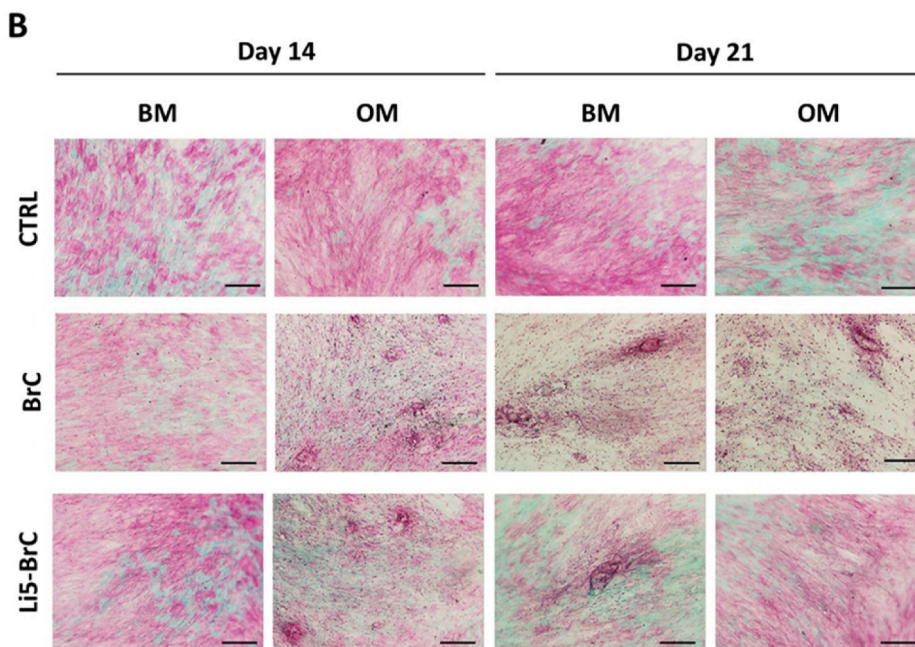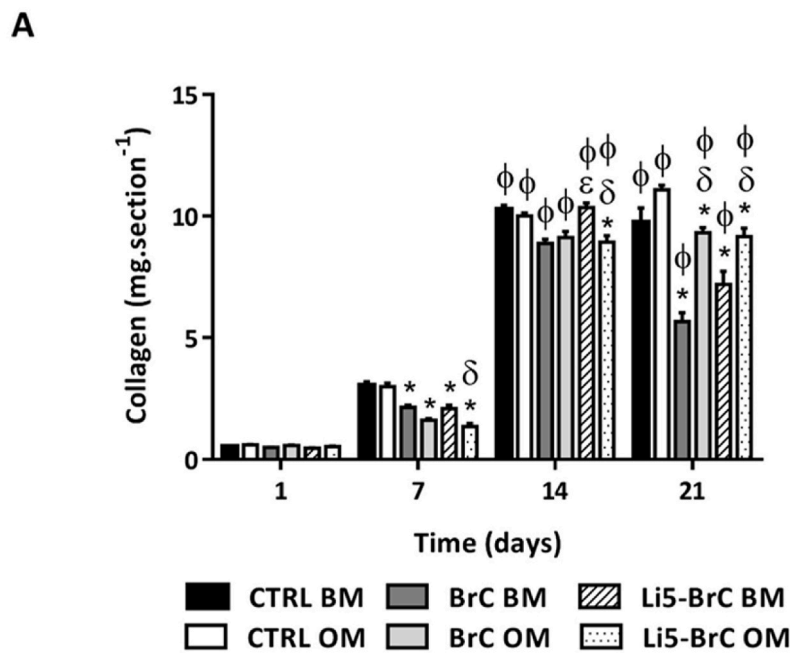
A

B

the Wnt/β-catenin pathway to enhance the proliferation and differentiation of osteoblasts [30].

One of the hallmarks of osteoblasts differentiation is the deposition of endogenous collagen [66]. Therefore, a Sirius Red/Fast Green Collagen Staining Kit was used to detect and quantify the presence of collagen (Fig. 9). This kit also enabled the detection of non-collagenous protein (Fig. 9 B, in green). As expected, at day 1, very low amounts of collagen were detected, increasing along the time of culture (Fig. 9 A). On day 7, lower collagen levels were observed in the presence of BrC and Li5–BrC compared to the CTRL. Nevertheless, on day 14, a significant increase was observed, reaching levels similar to CTRL. Finally, at day 21, higher values of collagen content were observed for the cement powders under OM conditions compared to BM, indicating and supporting the previous hypothesis that cells were differentiating along the osteoblastic lineage. Noteworthy, despite the lower levels of collagen

detected in CTRL conditions, no differences were observed between them, which may indicate that cells under CTRL conditions were probably less differentiated than cells cultured with the cements.

3.2.2.3. Genotypic and phenotypic evaluation of osteogenic-related markers. The differentiation of hASCs cultured in a basal and osteogenic-differentiation medium, with and without (CTRL) of BrC and Li5–BrC cement powders, was assessed by quantifying the mRNA levels of the osteogenic-related markers ALP, Col Iα, OPN, OCN, Runx, and BSP (Fig. 10 A). Analysis showed that cells expressed the typical osteogenic-related markers when they were cultured in all tested conditions. In general, the expression levels of ALP were higher after 21 days of culture and significantly higher at day 14 and day 21 in CTRL conditions, as compared with BrC and Li5–BrC at the same culture periods and conditions. When comparing BrC and Li5–BrC prepared in OM, significantly
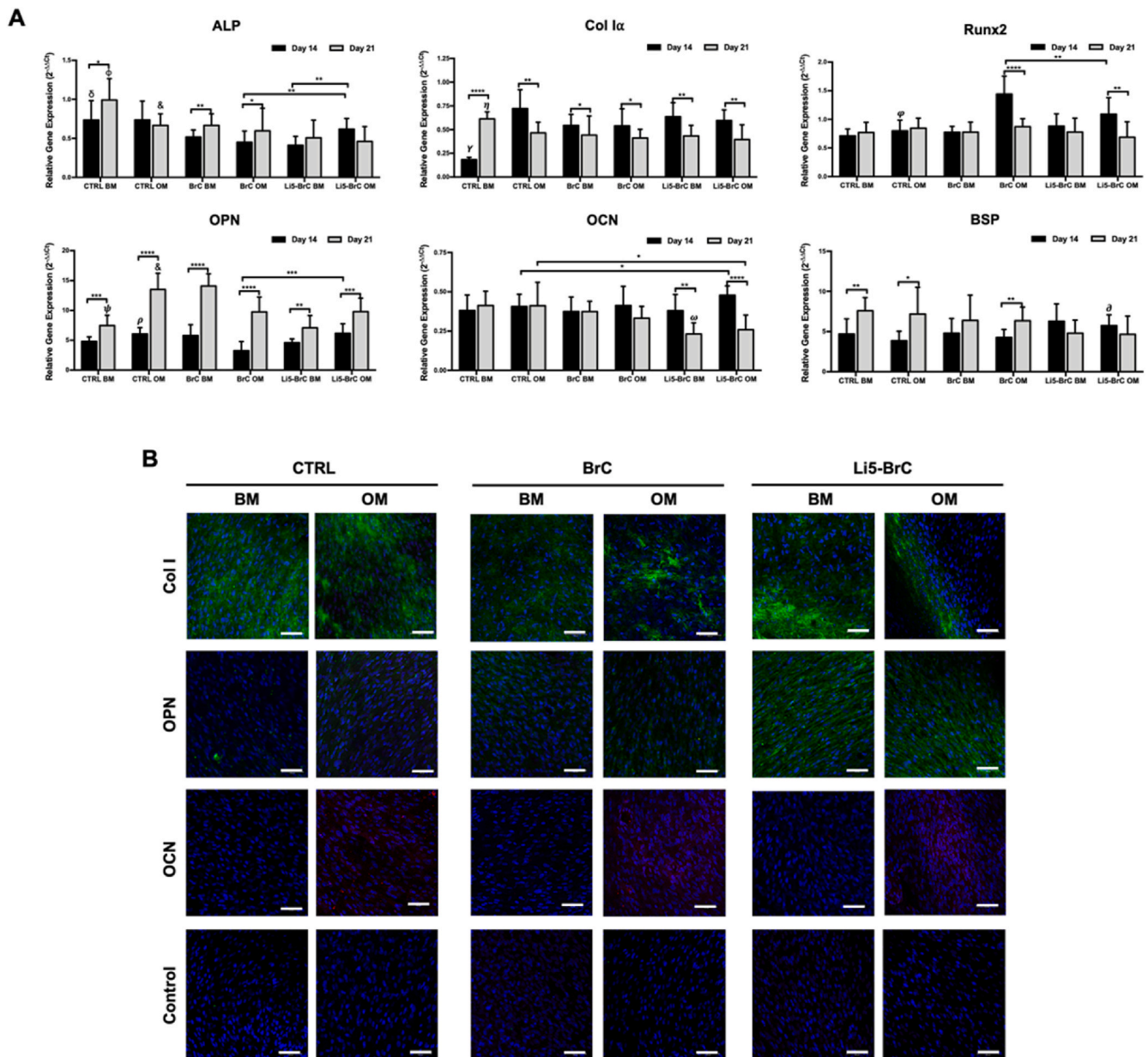
Fig. 10. Quantitative and qualitative expression of osteogenic-related markers expressed by hASCs after 14 and 21 days of culture in the presence and absence (CTRL) of BrC and Li5–BrC powders, in basal (BM) and osteogenic (OM)-differentiation medium. **(A)** Real-time PCR results of ALP, Col Iα, OPN, OCN, Runx, and BSP. δ denotes statistically significant when compared with BrC and Li5–BrC samples at the same culture period and under the same culture conditions (***p < 0.001). φ denotes statistically significant when compared with CTRL OM (**p < 0.01), BrC BM (**p < 0.01) and Li5–BrC BM (***p < 0.001) samples at the same culture period. & denotes statistically significant when compared with BrC (*p < 0.05) and Li5–BrC (**p < 0.01) samples at the same culture period and under the same culture conditions. γ denotes statistically significant when compared with CTRL OM, BrC BM, and Li5–BrC BM (****p < 0.0001) samples at the same culture period. η denotes statistically significant when compared with CTRL OM (**p < 0.01), BrC BM (**p < 0.01) and Li5–BrC BM (****p < 0.0001) samples at the same culture period. ρ denotes statistically significant when compared with CTRL BM (**p < 0.01) and BrC OM (***p < 0.001) samples at the same culture period. Ψ denotes statistically significant when compared with CTRL OM and BrC BM (****p < 0.0001) samples at the same culture period. ω denotes statistically significant when compared with CTRL (****p < 0.0001) and BrC (***p < 0.001) samples at the same culture period and under the same culture conditions. φ statistically significant when compared with BrC (****p < 0.0001) and Li5–BrC (**p < 0.01) samples at the same culture period and under the same culture conditions. ∂ denotes statistically significant when compared with CTRL and BrC (**p < 0.01) at the same culture period and under the same culture conditions. **(B)** Immunofluorescence analysis of the osteogenic-related markers and representative negative controls for immunofluorescence analysis. Nuclei are stained blue, Col I and OPN in green, and OCN in red (scale bar: 100 μm). (For interpretation of the references to color in this figure legend, the reader is referred to the Web version of this article.)

higher ALP levels were observed after 14 days of culture in the presence of Li5–BrC, showing the positive influence from Li⁺ incorporation in contact with differentiating cells [30]. This influence was also observed when compared to the Li5–BrC cultured in BM and OM, in which a significant up-regulation of ALP was observed at the earlier culture period on cells cultured in osteogenic conditions. Considering that ALP

is an early marker of bone differentiation, this result may indicate that the gradual release of Li⁺ potentiated ALP-induced osteogenic differentiation in osteogenic conditions [30,67]. These results also corroborate the ALP activity observed at days 14 and 21 (Fig. 8 A), in which osteogenic-induced hASCs presented significantly higher ALP activity compared to the cells cultured in BM. Col Iα is an early marker of

osteoblasts, which is in line with the significant up-regulation of Col Iα observed at day 14 in all conditions tested in OM [67]. The osteogenic potential of the cement powders was evidenced by the early and significant up-regulation of Col Iα observed on BrC and Li5–BrC cultured in standard BM.

The positive influence of ion-doped brushite cements on the early up-regulation of Col I in bone marrow stromal cells (mBMSCs) has been previously reported [51], and it is also in agreement with the significantly high levels of collagen content observed at day 14 and day 21 (Fig. 9 A). Runx2 is a transcription factor involved in bone development and is also considered an early marker of osteoblastic differentiation [68]. This is in agreement with the obtained results, in which a significantly higher expression of Runx2 was obtained at day 14 for cells cultured on BrC and Li5–BrC under OM, as compared to day 21. Interestingly, the expression of Runx2 was significantly higher on the BrC sample. Nevertheless, both BrC and Li5–BrC cement powders showed to be osteogenic inducers by the significant up-regulation of Runx2 on both conditions, as compared with the CTRL tested in OM. It is well reported that OPN, OCN, and BSP are late osteogenic differentiation markers, having a strong and crucial role in bone tissue mineralization [69,70]. This was shown by the significantly higher gene expression profile of OPN observed at day 21, as compared to day 14. In general, the conditions tested in OM benefit from OPN expression as compared to those tested in BM. Although at day 21 CTRL samples cultured in OM have shown significantly higher OPN expression than that observed on BrC and Li5–BrC samples, the positive influence of Li$^+$ doping was also confirmed by the significant up-regulation of OPN on Li5–BrC samples at the early time-point (day 14) as compared to BrC samples cultured in OM. A similar trend was observed for OCN gene expression, in which Li5–BrC showed significantly higher expression levels at day 14 compared to the CTRL tested in OM. Ultimately, the early and significantly higher expression of the late markers of osteogenic differentiation, OCN, and BSP on Li5–BrC samples tested in both OM and BM reinforces the osteogenic potential of Li-doped brushite cements [70].

Complementarily, the immunodetection of Col I, OPN, and OCN at the CTRL, BrC, and Li5–BrC samples was also evaluated (Fig. 10 B). Immunofluorescence images show an intense Col I protein expression after 21 days of culture in all tested conditions, especially in BM conditions with a uniformly distributed collagen deposition. This may also be related to the osteogenic differentiation of hASCs in osteogenic culture conditions, and it is consistent with the CoI Iα gene expression profile significantly up-regulated at day 14 compared to day 21. The phenotypic analysis of OPN showed the expression of this marker on BrC and Li5–BrC at day 21, both in BM and OM conditions, to a greater extent in the Li5–BrC. This result demonstrates the osteogenic potential of these materials and highlights the incorporation of Li$^+$ for increasing the *in vivo* bone density [71,72]. OCN analysis showed only a residual expression in all conditions tested in osteogenic differentiation medium but was completely absent in BM.

4. Conclusions

The present study provided a thorough physicochemical and biological characterization of Li$^+$-doped brushite cements. From a clinical perspective, the setting times are of chief importance. Both IST and FST of the investigated brushite cements decreased with increasing Li$^+$ content. They can be further optimized by adjusting the concentration of the setting retarder IP6, allowing the surgeon to close the defect shortly after cement placement in a better-controlled manner. ^{1}H NMR turned out as a versatile tool for the analysis of brushite cements, its combination with *in-situ* XRD being highly valuable for the thorough characterization of the setting reaction. No indications of Li$^+$ incorporation into brushite or monetite were found, while high amounts of Li$^+$ were detected in the pore water. This suggests a good availability of the ion in the biological environment, as its release will not directly depend on brushite or monetite degradation. Indeed, the major fraction of Li$^+$ was

released in PBS already after 1 d. Moreover, the cement powders showed no negative effects on hASCs, and the cells could recover the normal metabolic and proliferative levels. The immunodetection and gene expression profile of osteogenic-related markers highlights the potential of Li$^+$ incorporation for increasing bone density *in vivo*. Overall, the tunable properties of the developed Li$^+$-doped brushite cements and its osteogenic potential, evidenced by the significant up-regulation of Col Iα gene expression and ALP, show the promising benefits of these materials for bone regeneration and engineering processes.

Appendix A. Supplementary data

Supplementary data to this article can be found online at https://doi.org/10.1016/j.bioactmat.2021.12.025.

References

[1] A.D. Woolf, B. Pfleger, Burden of major musculoskeletal conditions, Bull. World Health Organ. 81 (2003) 646–656.
[2] M.W. Chapman, J.J. Rodrigo, Bone grafting, bone grafts substitutes, and growth factors, in: Chapman's Orthopaedic Surgery, Lippincott Williams & Wilkins, 2001.
[3] St John, T.A., et al., Physical and Monetary Costs Associated with Autogenous Bone Graft Harvesting. (1078-4519 (Print)).
[4] J.C. Banwart, R.S. Asher Ma Fau - Hassanein, and R.S. Hassanein, Iliac crest bone graft harvest donor site morbidity. A statistical evaluation. (362-2436 (Print)).
[5] S.V. Dorozhkin, Self-setting calcium orthophosphate formulations: cements, concretes, pastes and putties, Int. J. Mater. Chem. 1 (1) (2011) 1–48.
[6] W. Wang, K.W.K. Yeung, Bone grafts and biomaterials substitutes for bone defect repair: a review, Bioact Mater 2 (4) (2017) 224–247.
[7] J.C. Elliott, Structure and Chemistry of the Apatites and Other Calcium Orthophosphates, vol. 18, Elsevier, 2013.
[8] U. Gbureck, Injizierbare Calciumphosphat-Zemente als Knochenersatzwerkstoff in niedrig belasteten Bereichen des Skelettsystems, Verlag nicht ermittelbar, 2004.
[9] Z. Sheikh, et al., In vitro degradation and in vivo resorption of dicalcium phosphate cement based grafts, Acta Biomater. 26 (2015) 338–346.

[10] A.A. Mirtchi, J. Lemaître, E. Munting, Calcium phosphate cements: effect of fluorides on the setting and hardening of β-tricalcium phosphate-dicalcium phosphate-calcite cements, Biomaterials 12 (5) (1991) 505–510.

[11] M. Bohner, U. Gbureck, Thermal reactions of brushite cements. Journal of biomedical materials research Part B: applied biomaterials: an official journal of the society for biomaterials, The Japanese Society for Biomaterials, and The Australian Society for Biomaterials and the Korean Society for Biomaterials 84 (2) (2008) 375–385.

[12] J. Barralet, L. Grover, U. Gbureck, Ionic modification of calcium phosphate cement viscosity. Part II: hypodermic injection and strength improvement of brushite cement, Biomaterials 25 (11) (2004) 2197–2203.

[13] K. Hurle, et al., Hydration mechanism of a calcium phosphate cement modified with phytic acid, Acta Biomater. 80 (2018) 378–389.

[14] B.-T. Dong, et al., Lithium enhanced cell proliferation and differentiation of mesenchymal stem cells to neural cells in rat spinal cord, Int. J. Clin. Exp. Pathol. 8 (3) (2015) 2473.

[15] V. Graziani, et al., Zinc-releasing calcium phosphate cements for bone substitute materials, Ceram. Int. 42 (15) (2016) 17310–17316.

[16] X. Li, et al., Cu-loaded Brushite bone cements with good antibacterial activity and operability, J. Biomed. Mater. Res. B Appl. Biomater. 109 (6) (2021) 877–889.

[17] M. Fosca, J.V. Rau, V. Uskoković, Factors influencing the drug release from calcium phosphate cements, Bioact. Mater. 7 (2021) 341–363.

[18] X. Wang, et al., Calcium phosphate-based materials regulate osteoclast-mediated osseointegration, Bioact. Mater. 6 (12) (2021) 4517–4530.

[19] R. Enderle, et al., Influence of magnesium doping on the phase transformation temperature of β-TCP ceramics examined by Rietveld refinement, Biomaterials 26 (17) (2005) 3379–3384.

[20] J. Sarver, M. Hoffman, F. Hummel, Phase equilibria and tin-activated luminescence in strontium orthophosphate systems, J. Electrochem. Soc. 108 (12) (1961) 1103–1110.

[21] N. Matsumoto, et al., Preparation and characterization of β-tricalcium phosphate co-doped with monovalent and divalent antibacterial metal ions, Acta Biomater. 5 (8) (2009) 3157–3164.

[22] K. Spaeth, F. Goetz-Neunhoeffer, K. Hurle, Cu2+ doped β-tricalcium phosphate: solid solution limit and crystallographic characterization by rietveld refinement, J. Solid State Chem. 285 (2020) 121225.

[23] M. Yashima, et al., Crystal structure analysis of β-tricalcium phosphate Ca3 (PO4) 2 by neutron powder diffraction, J. Solid State Chem. 175 (2) (2003) 272–277.

[24] B. Dickens, L. Schroeder, W. Brown, Crystallographic studies of the role of Mg as a stabilizing impurity in β-Ca3 (PO4) 2. The crystal structure of pure β-Ca3 (PO4) 2, J. Solid State Chem. 10 (3) (1974) 232–248.

[25] K. Yoshida, et al., Substitution model of monovalent (Li, Na, and K), divalent (Mg), and trivalent (Al) metal ions for β-tricalcium phosphate, J. Am. Ceram. Soc. 89 (2) (2006) 688–690.

[26] L. Liu, et al., Lithium-containing biomaterials stimulate bone marrow stromal cell-derived exosomal miR-130a secretion to promote angiogenesis, Biomaterials 192 (2019) 523–536.

[27] L.A. Haro Durand, et al., *In* vitro human umbilical vein endothelial cells response to ionic dissolution products from lithium-containing 45S5 bioactive glass, Materials 10 (7) (2017) 740.

[28] S. Bose, et al., Understanding of dopant-induced osteogenesis and angiogenesis in calcium phosphate ceramics, Trends Biotechnol. 31 (10) (2013) 594–605.

[29] L. Chen, et al., 3D printing of a lithium-calcium-silicate crystal bioscaffold with dual bioactivities for osteochondral interface reconstruction, Biomaterials 196 (2019) 138–150.

[30] L. Li, et al., Lithium doped calcium phosphate cement maintains physical mechanical properties and promotes osteoblast proliferation and differentiation, J. Biomed. Mater. Res. B Appl. Biomater. 105 (5) (2017) 944–952.

[31] D. Jansen, et al., Does Ordinary Portland Cement contain amorphous phase? A quantitative study using an external standard method, Powder Diffr. 26 (1) (2011) 31–38.

[32] K. Hurle, J. Neubauer, F. Goetz-Neunhoeffer, Hydration enthalpy of amorphous tricalcium phosphate resulting from partially amorphization of β-tricalcium phosphate, BioNanoMaterials 18 (3–4) (2017).

[33] N.A. Curry, D.W. Jones, Crystal structure of brushite, calcium hydrogen orthophosphate dihydrate: a neutron-diffraction investigation, J. Chem. Soc. Inorg. Phys. Theor. (1971) 3725–3729, 0.

[34] M. Catti, G. Ferraris, A. Filhol, Hydrogen bonding in the crystalline state. CaHPO4 (monetite), P\\overline{1} or P1? A novel neutron diffraction study, Acta Crystallogr. B 33 (4) (1977) 1223–1229.

[35] L.W. Schroeder, E. Prince, B. Dickens, Hydrogen bonding in Ca(H2PO4)2.H2O as determined by neutron diffraction, Acta Crystallogr. B 31 (1) (1975) 9–12.

[36] S. Bergold, F. Goetz-Neunhoeffer, J. Neubauer, Quantitative analysis of C–S–H in hydrating alite pastes by in-situ XRD, Cement Concr. Res. 53 (2013) 119–126.

[37] D. Ectors, et al., In situ H-1-TD-NMR: quantification and microstructure development during the early hydration of alite and OPC, Cement Concr. Res. 79 (2016) 366–372.

[38] S. Bergold, F. Goetz-Neunhoeffer, J. Neubauer, Mechanically activated alite: new insights into alite hydration, Cement Concr. Res. 76 (2015) 202–211.

[39] G. Berger, et al., New characterization of setting times of alkali containing calcium phosphate cements by using an automatically working device according to gillmore needle test, Key Eng. Mater. 309–311 (2006) 825–828.

[40] S. Pina, et al., Biological responses of brushite-forming Zn- and ZnSr- substituted beta-tricalcium phosphate bone cements, Eur. Cell. Mater. 20 (2010) 162–177.

[41] N. Matsumoto, et al., Dissolution mechanisms of β-tricalcium phosphate doped with monovalent metal ions, J. Ceram. Soc. Jpn. 118 (1378) (2010) 451–457.

[42] K. Yoshida, et al., Sintering and mechanical properties of β-tricalcium phosphates doped with alkali metal and alkali earth metal ions, Phosphorus Research Bulletin 13 (2002) 271–274.

[43] K. Yoshida, et al., Effect of substitutional monovalent and divalent metal ions on mechanical properties of β-tricalcium phosphate, J. Am. Ceram. Soc. 88 (8) (2005) 2315–2318.

[44] R.D. Shannon, Revised effective ionic radii and systematic studies of interatomic distances in halides and chalcogenides, Acta Crystallogr. Sect. A Cryst. Phys. Diffr. Theor. Gen. Crystallogr. 32 (5) (1976) 751–767.

[45] A. Dosen, R.F. Giese, Thermal decomposition of brushite, CaHPO4· 2H2O to monetite CaHPO4 and the formation of an amorphous phase, Am. Mineral. 96 (2–3) (2011) 368–373.

[46] D.A. Kulik, et al., GEM-Selektor geochemical modeling package: revised algorithm and GEMS3K numerical kernel for coupled simulation codes, Comput. Geosci. 17 (1) (2013) 1–24.

[47] T. Wagner, et al., GEM-Selektor geochemical modeling package: TSolMod library and data interface for multicomponent phase models, Can. Mineral. 50 (5) (2012) 1173–1195.

[48] N. Matsumoto, et al., Thermal stability of β-tricalcium phosphate doped with monovalent metal ions, Mater. Res. Bull. 44 (9) (2009) 1889–1894.

[49] S. Vahabzadeh, V.K. Hack, S. Bose, Lithium-doped β-tricalcium phosphate: effects on physical, mechanical and in vitro osteoblast cell–material interactions, J. Biomed. Mater. Res. B Appl. Biomater. 105 (2) (2017) 391–399.

[50] S. Vahabzadeh, et al., Effects of cobalt on physical and mechanical properties and in vitro degradation behavior of brushite cement, J. Occup. Med. (71) (2019) 315–320.

[51] K. Hurle, et al., Ion-doped brushite cements for bone regeneration, Acta Biomater. 123 (2021) 51–71.

[52] A.T. Saleh, L.S. Ling, R. Hussain, Injectable magnesium-doped brushite cement for controlled drug release application, J. Mater. Sci. 51 (16) (2016) 7427–7439.

[53] G. Li, et al., Fe-doped brushite bone cements with antibacterial property, Mater. Lett. 215 (2018) 27–30.

[54] J.V. Rau, et al., Silver-doped calcium phosphate bone cements with antibacterial properties, J. Funct. Biomater. 7 (2) (2016).

[55] A. Taha, et al., Strontium doped injectable bone cement for potential drug delivery applications, Materials science & engineering. C, Materials for biological applications 80 (2017) 93–101.

[56] G. Vereecke, J. Lemaître, Calculation of the solubility diagrams in the system Ca (OH) 2-H3PO4-KOH-HNO3-CO2-H2O, J. Cryst. Growth 104 (4) (1990) 820–832.

[57] T. Manninger, et al., Accelerating effect of Li2CO3 on formation of monocarbonate and Al-hydroxide in a CA-cement and calcite mix during early hydration, Cement Concr. Res. 126 (2019) 105897.

[58] S. Rodger, D. Double, The chemistry of hydration of high alumina cement in the presence of accelerating and retarding admixtures, Cement Concr. Res. 14 (1) (1984) 73–82.

[59] M. Bohner, H. Merkle, t.J. Lemai, In vitro aging of a calcium phosphate cement, J. Mater. Sci. Mater. Med. 11 (3) (2000) 155–162.

[60] L.C. Chow, Calcium Phosphate Cements: Chemistry, Properties, and Applications, MRS Online Proceedings Library (OPL), 1999, p. 599.

[61] F. Tamimi, Z. Sheikh, J. Barralet, Dicalcium phosphate cements: brushite and monetite, Acta Biomater. 8 (2) (2012) 474–487.

[62] L.M. Grover, et al., Temperature dependent setting kinetics and mechanical properties of β-TCP–pyrophosphoric acid bone cement, J. Mater. Chem. 15 (46) (2005) 4955–4962.

[63] M. Schamel, et al., Cu2+, Co2+ and Cr3+ doping of a calcium phosphate cement influences materials properties and response of human mesenchymal stromal cells, Mater. Sci. Eng. C 73 (2017) 99–110.

[64] K. Marycz, et al., Li+ activated nanohydroxyapatite doped with Eu3+ ions enhances proliferative activity and viability of human stem progenitor cells of adipose tissue and olfactory ensheathing cells. Further perspective of nHAP:Li+, Eu3+ application in theranostics, Mater. Sci. Eng. C 78 (2017) 151–162.

[65] P. Clément-Lacroix, et al., Lrp5-independent activation of Wnt signaling by lithium chloride increases bone formation and bone mass in mice, Proc. Natl. Acad. Sci. U. S. A. 102 (48) (2005) 17406–17411.

[66] A. Rutkovskiy, K.-O. Stensløkken, I.J. Vaage, Osteoblast differentiation at a glance, Medical science monitor basic research 22 (2016) 95–106.

[67] J. Aberg, et al., Premixed acidic calcium phosphate cement: characterization of strength and microstructure, J. Biomed. Mater. Res. B Appl. Biomater. 93 (2) (2010) 436–441.

[68] Low osteogenic differentiation potential of placenta-derived mesenchymal stromal cells correlates with low expression of the transcription factors Runx2 and Twist2, Stem Cell. Dev. 22 (21) (2013) 2859–2872.

[69] M. Alicka, et al., Lithium ions (Li+) and nanohydroxyapatite (nHAp) doped with Li + enhance expression of late osteogenic markers in adipose-derived stem cells. Potential theranostic application of nHAp doped with Li+ and co-doped with europium (III) and samarium (III) ions, Mater. Sci. Eng. C 99 (2019) 1257–1273.

[70] G. Bouet, et al., The impairment of osteogenesis in bone sialoprotein (BSP) knockout calvaria cell cultures is cell density dependent, PLoS One 10 (2) (2015), e0117402.

[71] B.-T. Dong, et al., Lithium enhanced cell proliferation and differentiation of mesenchymal stem cells to neural cells in rat spinal cord, Int. J. Clin. Exp. Pathol. 8 (2015) 2473–2483.

[72] M. Ali, et al., Lithium-containing surface pre-reacted glass fillers enhance hDPSC functions and induce reparative dentin formation in a rat pulp capping model through activation of Wnt/β-catenin signaling, Acta Biomater. 96 (2019) 594–604.